Intertwined $Cu_3V_2O_7(OH)_2 \cdot 2H_2O$ nanowires/carbon fibers composite: a new anode with high rate capability for sodium-ion batteries

Liying Liang[a], Yang Xu[a], Xin Wang[b], Chengliang Wang[a], Min Zhou[a], Qun Fu[b], Minghong Wu[b], Yong Lei [a,*]

[a] *Institute for Physics and IMN MacroNano®, Technical University of Ilmenau, Ilmenau 98693, Germany. Fax: +49(0)3677 69-3746; Tel: +49(0)3677 69-3748; E-mail: yong.lei@tu-ilmenau.de*

[b] *Institute of Nanochemistry and Nanobiology, School of Environmental and Chemical Engineering, Shanghai University, Shanghai 200444, P. R. China.*

Abstract

Sodium-ion batteries (SIBs) have recently attracted intensive attentions as a potential alternative to LIBs for large-scale energy storage applications. However, one of the major challenges to the commercialization of SIBs is the limited choice of anode materials that can offer high rate capability. In this regard, we report intertwined $Cu_3V_2O_7(OH)_2 \cdot 2H_2O$ nanowires/carbon fibers composite, fabricated by a facile hydrothermal method, as the anode material for SIBs. It shows s a highly reversible Na-ion storage capacity of 287.4 mAh g^{-1} after 50 cycles at a large current density of 0.5 A g^{-1}, and excellent rate performance of delivering 206.5 and 127.7 mAh g^{-1} after 50 cycles at high current densities of 5 and 10 A g^{-1}, respectively. The promising performance is ascribed to both the crystal structure of $Cu_3V_2O_7(OH)_2 \cdot 2H_2O$ with a large interlayer spacing, and unique intertwined network morphology of CuVOH-NWs/CFs composite in which CuVOH-NWs and CFs synergistically functioned. This work will pave a way to develop more metal vanadates materials as anodes for high-performance SIBs.

Keywords: metal vanadates materials, intertwined network, carbon fibers, anode, sodium-ion batteries

1. Introduction

Lithium-ion batteries (LIBs) have been widely employed as power sources for portable electronic devices. However, there are still great concerns about the safety, and lithium's cost and continued availability.[1-4] Therefore, as a potential alternative to LIBs, sodium-ion batteries (SIBs) have recently attracted intensive attentions, since sodium is much cheaper, safer, and more environmentally benign than lithium.[5] Due to larger radius of Na^+ than that of Li^+, it is difficult to find a suitable electrode material to allow reversible and rapid Na ions insertion and extraction at high rates.[6,7] Improvements have been achieved for SIB cathode materials with this regard,[8-11] however, less have been devoted on the side of anode materials. Several carbonaceous materials have been proposed, however, due to poor intercalation property for large Na ions, limited capacities at high rate are shown.[12-14] Another emerging anode of TiO_2 also has been widely investigated.[15-17] Although they generally show stable Na-ion storage reversibility, their capacities at high rates are not satisfactory. For example, Kim *et al.* reported carbon-coated anatase nanorod TiO_2 that showed a stable capacity of about 190 mAh g^{-1} at the current density of 10 mA g^{-1}, however, the capacity at 1.65 A g^{-1} was only around 88 mAh g^{-1}.[15] Metallic Sb, Sn, Pb, Ge, and their alloys based materials have been recently presented to be promising anodes due to their large theoretical Na-storage capacities.[18] However, the practical applications of alloy-based materials are mainly hindered by the massive volume changes (100–400% upon full sodiation) which results in mechanical destruction of the electrodes, then decreasing the cycling life and rate capability of electrodes.[18]

It is well-known that in order to achieve high rate performance, three important elements are indispensable, which are high ion diffusion, fast electron transport, and stable electrode structure. In this regard, we propose a rational electrode design: intertwined $Cu_3V_2O_7(OH)_2 \cdot 2H_2O$ nanowires/carbon fibers (CuVOH-NWs/CFs) composite as a SIB anode with promising rate capability. As for this design, there are some critical features that should be emphasized. One is why we choose $Cu_3V_2O_7(OH)_2 \cdot 2H_2O$ nanowires (CuVOH-NWs) as the host material for SIBs. Firstly, volborthite, $Cu_3V_2O_7(OH)_2 \cdot 2H_2O$ is a rare copper vanadate mineral. Vanadium-based mixed metal oxides have been extensively studied for energy storage, since they can offer much wider potential window deriving from various oxidation states of both metal elements and higher energy density, together with their low cost, and wide existence in nature.[19] Secondly, vanadium-based materials reveal layered nature and excellent kinetics, which are greatly beneficial for large Na^+ insertion/extraction.[20,21] Benefit from this point, some vanadium-based materials have been recently reported as cathodes for SIBs, and obtaining good electrochemical performance.[22-26] For example, Hartung *et al.* fabricated a novel SIBs cathode, $Na_{2.55}V_6O_{16} \cdot 0.6H_2O$, that showed the initial capacities of 217 mAh g^{-1} for 20 mA g^{-1}, and significant capacities even at current densities up to 800 mA g^{-1}.[22] Su *et al.* designed a single-crystalline bilayered V_2O_5 nanobelts with a large interlayer spacing (11.53 Å), which exhibited a stable capacity of 180 mAh g^{-1} after 100 cycles at a current density of 80 mA g^{-1} and excellent rate capability.[25] However, vanadium-based materials as SIBs anodes have not been reported. Therefore, in this

work, we fabricated $Cu_3V_2O_7(OH)_2 \cdot 2H_2O$ as a promising anode for SIBs. Just like other vanadium-based materials, $Cu_3V_2O_7(OH)_2 \cdot 2H_2O$ also has a layered crystal structure. As clearly seen in Scheme 1c (the crystal structure of $Cu_3V_2O_7(OH)_2 \cdot 2H_2O$), the $CuO_4(OH)_2$ octahedral units are edge-shared with each other to form $Cu_3O_6(OH)_2$ layers in the *ab* plane, separated by V_2O_7 pillars and unligated water molecules in the *c* direction, resulting in a layered structure which is a potential advantage to allow facile Na ions insertion and extraction.[25-27] It is widely recognized that the larger Na^+ with higher ionization potential than that of Li^+, thus a more open framework of SIBs material is required, in which Na ions can move reversibly with acceptable mobility.[13,28] $Cu_3V_2O_7(OH)_2 \cdot 2H_2O$ exactly possesses a large interlayer spacing (d(001)=7.187 Å), which can accommodate the large Na ions insertion and extraction. Thirdly, the construction of one dimensional (1D) nanowires is largely beneficial for shortened Na ion diffusion length. On the other hand, it is why we build the intertwined hybrid structure. Fast and effective electron transport is the precondition of high rate capability. Highly conductive carbon fibers (CFs) can provide sufficient electrons for $Cu_3V_2O_7(OH)_2 \cdot 2H_2O$ nanowires, thus improving the electrical conductivity of the composite. Meanwhile, numerous interconnected pore channels created by intertwined network facilitate the access of electrolyte and electrode, then improving Na ion accessibility at high rates.[29-31]

Herein, we fabricated intertwined $Cu_3V_2O_7(OH)_2 \cdot 2H_2O$ nanowires/carbon fibers composite by using a facile hydrothermal method, as shown in Scheme 1a. Within expectation, when used as anode for SIBs for the first time, CuVOH-NWs/CFs

composite revealed highly reversible Na-ion storage capability, and excellent rate cycle performance of delivering high capacities of 206.5 and 127.7 mAh g^{-1} after 50 cycles at high current densities of 5 and 10 A g^{-1}, respectively.

2. Experimental

2.1 Materials Synthesis

$Cu_3V_2O_7(OH)_2 \cdot 2H_2O$/carbon fibers composite was synthesized by one-pot hydrothermal method using aqueous $CuCl_2 \cdot 2H_2O$ and NH_4VO_3 precursors in the presence of pre-treated hydrophilic carbon fibers. Firstly, carbon fibers were functionalized by HNO_3 and H_2SO_4 at 120 ℃ for 2 h and then washed with distilled water and ethanol. Secondly, one-pot hydrothermal method similar to one reported by Zhang *et al.*[32] was used to synthesize $Cu_3V_2O_7(OH)_2 \cdot 2H_2O$/carbon fibers composite. Briefly, 0.2046 g $CuCl_2 \cdot 2H_2O$ was dissolved in 15 mL distilled water containing 0.062 g functionalized carbon fibers (33% of theoretical amount of $Cu_3V_2O_7(OH)_2 \cdot 2H_2O$ fabricated from 0.2046 g $CuCl_2 \cdot 2H_2O$ by weight) and then was vigorously stirred. At the same time, 0.047 g NH_4VO_3 was dissolved in another 15 mL distilled water at 80 ℃. After that, the NH_4VO_3 solution was added slowly to the $CuCl_2 \cdot 2H_2O$ suspension with stirring. After stirring for 30 min, the resulting precursor suspension was transferred to a 50 mL autoclave and kept in an oven at 180 ℃ for 24 h. Finally, the product was filtered and rinsed with distilled water and ethanol several times and dried at 60 ℃ for 12 h. For comparison, pure $Cu_3V_2O_7(OH)_2 \cdot 2H_2O$ nanowires were also prepared by a similar procedure to that described above in the

absence of functionalized carbon fibers .

2.2 Materials characterization

X-ray diffraction (XRD) patterns were conducted on a MAXima-X XRD-7000 with Cu-Ka radiation. SEM and TEM images were taken on a Hitachi S4800 instrument with voltages of 5 kV and 30 kV, respectively. HRTEM images were tested by using Tecnai 20 S-Twin from Philips. X-ray photoelectron spectroscopy (XPS) measurements were carried out using the ESCALAB 250Xi instrument equipped with an Al-Ka X-ray source at pass energy of 150.0 eV.

2.3 Electrochemical measurements

Electrochemical measurements were performed using two electrode coin cells with sodium metal as the counter and reference electrode. The working electrode was composed of 70% active materials, 20% acetylene black, and 10% sodium carboxymethyl cellulose (CMC) binder by weight. The above mixture was pressed onto a copper foil which served as a current collector. The electrode was dried at 120 ℃ in vacuum for 12 h. The mass loading of the active material in each coin cell was around 1.2 mg cm^{-2}. The coin batteries were assembled in a nitrogen-filled glove box with a glass fiber separator (Whatman, GFB/55) and the electrolyte of 1 M $NaClO_4$ in EC: PC (1:1 by volume). Cyclic voltammetry (CV) was tested at a scan rate of 0.1 mV s^{-1} with the voltage range of 0.01-3.0 V (*vs.* Na^+/Na) on a BioLogic VSP potentiostat. Galvanostatic discharge–charge measurements were tested at a potential range of 0.01-3.0 V using a LAND-CT2001A test system (Wuhan, China) at

room temperature. The cell coin was firstly discharged to 0.01 V at a constant current, and then charged to 3.0 V at a constant current. After constant current charge, a short constant voltage charge process (3.0 V) was taken.

3. Result and Discussion

The crystal phase of the products was analyzed by X-ray diffraction (XRD). Fig. 1a displays the XRD patterns of bare CFs, pure CuVOH-NWs, and CuVOH-NWs/CFs composite. All diffraction peaks of pure CuVOH-NWs can be readily indexed to the pure phase of $Cu_3V_2O_7(OH)_2 \cdot 2H_2O$ with the monoclinic structure (JCPDS No. 80-1170). For CuVOH-NWs/CFs composite, the analysis of its spectrum is consistent with that of CuVOH-NWs except for an additional peak appearing at 2 θ of 26.4°. Such peak originates from the (002) plane of (CFs). No peaks from other phases have been detected, suggesting the high purity of the composite.

To determine the chemical composition and valence state of CuVOH-NWs/CFs composite, X-ray photoelectron spectroscopy (XPS) analyses were conducted. No peaks of other elements except Cu, V, O, and C were observed in the survey spectrum (Fig. 1b), again indicating the high purity of this composite. The Cu 2p XPS spectrum of the composite shows the peaks at 934.87 and 954.89 eV, corresponding to the Cu 2p3/2 and Cu 2p1/2 characteristic peaks of CuVOH-NWs (Fig. 1c). As for the peak at 942.94 eV, it can be assigned to a typical character of Cu^{2+}. In Fig. 1d, two separate peaks observed at 517.34 and 524.76 eV are ascribed to V^{5+} 2p3/2 and 2p1/2, respectively.

The morphology and structure of the CuVOH-NWs/CFs composite were investigated by scanning electron microscopy (SEM) and transmission electron microscopy (TEM). Fig. 2a shows the overall SEM image of CuVOH-NWs/CFs composite, consisting of CuVOH-NWs and CFs to form an intertwined network, in which they are homogeneously dispersed over a wide area. The obvious difference between them is that CFs are round, whereas CuVOH-NWs are flat. A close observation of the composite is demonstrated in Fig. 2b, where CuVOH-NWs interconnected with each other, forming a porous network architecture in morphology, while CFs penetrate through the network of CuVOH-NWs. Meanwhile, it is clearly seen the hierarchical porous channels created by the network, which is greatly significant for effective electrolyte transport and improved Na ion accessibility. As a reference sample, we also investigated the SEM image of pure CuVOH-NWs, as shown in Fig. 2c. The growth mechanism for CuVOH-NWs is an Ostwald ripening and splitting process.[32] The unique intertwined network structure of CuVOH-NWs/CFs composite is further confirmed by TEM (Fig. 2d) in which CuVOH-NWs and CFs are intertwined together, benefiting to the electron transfer and then increased electrical conductivity of the composite. The transport mechanism of Na ions and electrons in the composite is presented in Scheme 1b. Fig. 2e presents CuVOH-NWs with one-dimensional (1D) structure with the diameter of around 120 nm. The corresponding selected area electron diffraction (SEAD) patterns in Fig. 2e inset prove that CuVOH-NWs are single crystalline. High resolution TEM (HRTEM) image in Fig. 2f clearly reveals the clear lattice fringe of CuVOH-NWs with a lattice

spacing of 0.718 nm, which is in accordance with the (001) crystal planes. The lattice fringe of (001) planes, combined with SAED patterns (Fig. 2e inset), we may deduce that CuVOH-NWs exhibit a preferred orientation in the [001] direction, which is in a good agreement with XRD patterns on this point. Moreover, such clear lattice fringe indicates its typical layered structure, and the large interlayer spacing (0.718 nm) of $Cu_3V_2O_7(OH)_2 \cdot 2H_2O$ will offer an open framework for Na^+ moving reversibly with acceptable mobility. Therefore, a promising electrochemical performance is highly expected.

To evaluate the electrochemical performance of CuVOH-NWs/CFs composite as anodes for SIBs, a series of electrochemical measurements were conducted. Fig. 3 shows cyclic voltammograms (CVs) of the CuVOH-NWs/CFs composite anode for the initial three cycles between 0.01 and 3.00 V (*vs.* Na^+/Na) at a scan rate of 0.1 mV s^{-1}. In the first cathodic scan, there are three reduction peaks located at 1.30, 0.87, and 0.38 V corresponding to the insertion of Na^+ into CuVOH-NWs. Two oxidation peaks at 1.45 and 2.38 V are attributed to the extraction of Na^+ from CuVOH-NWs. The oxidation peak at 2.85 V in the first cycle and disappearing in the following scan derives from Cu_xO_y which forms during the storage of commercial copper foils. Its contribution to the total capacity is negligible, and this phenomenon has been previously reported.[33,34] Another one pair of peaks at about 0.01/0.08 V (not in the CV of pure CuVOH-NWs, Fig. S1) can be assigned to the Na^+ insertion/extraction into/from CFs, in accord with CVs of bare CFs (Fig. S2). After the activation process during the first scan, the peak positions and intensities remain stable for the

subsequent ones, suggesting the occurrence of stable oxidation/reduction reactions and high reversibility of this electrode.

To further understand the sodium storage mechanism, XPS spectra were conducted for CuVOH-NWs/CFs composite at different cell voltages to investigate the change of valence states upon sodium insertion/extraction. In the first discharge process (Fig. 4), when the electrode was discharged to 1.30 (a) and 0.87 V (b), the peaks for Cu 2p3/2 and Cu 2p1/2 can be divided into two components. Besides the existence of Cu^{2+}, two doublet peaks of Cu 2p at the binding energies of 932.6 eV (Cu 2p3/2) and 952.7 eV (Cu 2p1/2), are attributed to Cu^{+}. Meanwhile, the peaks for V 2p also can be deconvoluted into two parts. The binding energies of 516.6 and 523.5 eV confirm the formation of V^{4+}. Moreover, an increase in the area of the peaks for V^{4+} is observed, indicating that most of V^{5+} is reduced to V^{4+} upon discharging. When the electrode was deeply discharged to 0.38 V (c), two new peaks located at 932.3 and 951.4 eV for Cu 2p can be indexed to Cu^{0} 2p3/2 and 2p1/2, implying that the Cu^{+} is further reduced to metallic Cu with discharging. Meanwhile, as for V region, two new peaks observed at 515.7 and 522.5 eV are showing, which are assigned to V^{3+} 2p3/2 and 2p1/2, accompanied by the decreased area of V^{5+} peaks, indicating almost complete reduction V^{5+} to V^{4+} and partial reduction of V^{4+} to V^{3+}. At the end of discharge process (d), three different Cu valences and V valences still are observed.

XPS spectra at different voltages in the first charge process were also conducted, as shown in Fig. S3. At the end of charge process (g), three sets of peaks indexed to Cu^{2+}, Cu^{+}, Cu^{0} still can be observed in the Cu region. The gradual increased peak areas of

Cu^{2+} and Cu^{+} indicate that the oxidation from Cu^{0} to Cu^{+} and Cu^{2+} progressed continuously through the whole charge process with consecutive sodium extraction. However, it is noticeable that the oxidation was not complete and partial copper is left at the end of charge process, which could explain the difference between discharge and charge capacities. This phenomenon is similar to some metal vanadates electrodes, such as $Ag_2V_4O_{11}$[35], β-$AgVO_3$[29], and CuV_2O_6[36]. With regard to V region, gradual oxidation from V^{3+}, V^{4+} to V^{5+} continuously proceeded, and was completed at the end of charge process, in which no peak belonging to V^{3+} and V^{4+} can be observed.

The cycle performance of CuVOH-NWs/CFs composite anode was investigated at a high current density of 0.5 A g^{-1}, and pure CuVOH-NWs and bare CFs were also conducted at the same condition as reference samples, as shown in Fig. 5a. In the case of CuVOH-NWs/CFs composite, the first Coulombic Efficiency (CE) is 71.4%, while stabilizing at around 97% during the following cycles, indicating facile and efficient ions and electrons transport in this electrode.[37,38] The second discharge capacity of the composite is 398.6 mAh g^{-1}, and a high capacity of 287.4 mAh g^{-1} after 50 cycles still is obtained. For the same current density, the capacity of CuVOH-NWs/CFs composite is among the highest values for SIB anodes.[15,28,39-45] In contrast, much lower capacities are observed for pure CuVOH-NWs (50th discharge capacity of 174.2 mAh g^{-1}) and bare CFs (50th discharge capacity of 81.4 mAh g^{-1}). In addition, CuVOH-NWs show a much more capacity decay than CuVOH-NWs/CFs composite. The discharge capacity dramatically decreases from 336.8 mAh g^{-1} to 174.2 mAh g^{-1}

after 50 cycles, with the capacity retention of 51.2% (72.1% for CuVOH-NWs/CFs composite). These differences prove that intertwined CuVOH-NWs/CFs composite could successfully improve electronic/ionic transport within the electrode, resulting in enhanced electrochemical performance, which is further supported by the results of EIS (Fig. 5b) where the charge-transfer resistance of CuVOH-NWs/CFs composite (19.65 Ω) is lower than that of pure CuVOH-NWs (33.14 Ω). Furthermore, it is striking to note that the capacity of CuVOH-NWs/CFs composite is much higher than the sum of contributions from CuVOH-NWs and CFs constitutes, indicating that the strong synergistic effect between CuVOH-NWs and CFs plays a significant role in improving the capacity and cycling stability of CuVOH-NWs/CFs composite.

Galvanostatic charge/discharge curves of CuVOH-NWs/CFs composite anode between 0.01 and 3.0 V (*vs.* Na^+/Na) at a current density of 0.5 A g^{-1} are shown in Fig. 5c. In agreement with the above CV results, the charge/discharge processes present multiple redox plateaus, reflecting the steps of Na^+ insertion/extraction into/from CuVOH-NWs/CFs composite. The first charge and discharge capacities are approximately 335.2 and 469.5 mAh g^{-1}, respectively, resulting in an initial CE of 71.4%. The initial irreversible capacity loss of CuVOH-NWs/CFs composite is due to the inevitable formation of SEI films, decomposition of electrolyte, and partial irreversibility of copper oxidation. It is worth noting that both charge and discharge profiles demonstrate much less change from the second to the 50th cycles than pure CuVOH-NWs (Fig. S4), again indicating relatively stable cycling of intertwined CuVOH-NWs/CFs composite. With regard to bare CFs (Fig. S5), except the first two

cycles, both charge and discharge profiles are perfectly reproducible, due to its great electrical conductivity.

In addition to the high capacity and good cycling stability, CuVOH-NWs/CFs composite anode also reveals excellent rate performance (Fig. 5d). The rate cycle performance of CuVOH-NWs/CFs anode up to 10 A g^{-1} was studied in the potential window of 0.01 to 3 V. It is clearly found that even when the current density is increased to 10 from 0.1 A g^{-1} with 100 times, the capacity does not show a sharp drop up to the 50th cycle. In detail, the 50th cycle discharge capacities are 312.6, 287.4, 251.9, 206.5, and 127.7 mAh g^{-1} at current densities of 0.1, 0.5, 1, 5, and 10 A g^{-1}, respectively. To our best knowledge, such a rate capability shows clear advantages over those of some reported organic and inorganic Na-ion anode materials, as shown in Table 1. The CuVOH-NWs/CFs composite anode can be charged and discharged at such high rates with such high capacities, which are highly desired for practical applications.

The excellent electrochemical performance of CuVOH-NWs/CFs composite is attributed to the following factors. (i) As aforementioned, $Cu_3V_2O_7(OH)_2 \cdot 2H_2O$ possesses a layered structure, in which $Cu_3O_6(OH)_2$ layers were separated by V_2O_7 pillars and unligated water molecules, leading to suitable gaps in this crystal structure. The gaps constitute a channel, which is largely favourable for Na^+ to transport through the plane. This point has also been proved in SIBs cathodes.[22,25,26] In addition, it is reasonable to expect that the V_2O_7 pillars between $Cu_3O_6(OH)_2$ layers are in favor of alleviating the possible structural collapse upon cycling.[46]; (ii) the

unique intertwined structure fully shows the synergistic effect of CuVOH-NWs and CFs. CuVOH-NWs offer high charge storage capacity deriving from shortened Na ions diffusion length, while CFs provide fast and sufficient electrons, which will be greatly beneficial to cycling stability and rate capability. Moreover, the 3D intertwined network creates numerous interconnected pore channels which facilitate the access of electrolyte and electrode, thus improving Na ion accessibility at high rates. The intertwined network also reduces the stress caused by the cracking of the structure during repeated charge/discharge processes, and greatly decreases the degradation of the electrode. As shown in Fig. 6, the intertwined network still is maintained after 100 cycles at a high current density of 0.5 A g^{-1}. All these advantages induce highly reversible Na-ion storage capability, and excellent rate cycle performance of CuVOH-NWs/CFs anode.

4. Conclusions

In summary, intertwined CuVOH-NWs/CFs composite was reasonably designed and fabricated as an anode for SIBs, for the sake of improving the battery performance, especially the current challenge of rate capability. As expected, the composite is proved to be a promising anode with enhanced electrochemical performance, showing a highly reversible Na-ion storage capacity of 287.4 mAh g^{-1} after 50 cycles at a large current density of 0.5 A g^{-1}. The capacity is among the highest values for SIB anodes at the same current density. Notably, the composite anode revealed a superior rate capability with reversible capacities of 206.5 and 127.7 mAh g^{-1} after 50 cycles at high current densities of 5 and 10 A g^{-1}, respectively, which is better than those of

majority of SIB anodes. The excellent electrochemical properties described herein can be ascribed to both the crystal structure of $Cu_3V_2O_7(OH)_2 \cdot 2H_2O$ with a large interlayer spacing, and unique intertwined network morphology of CuVOH-NWs/CFs composite in which CuVOH-NWs and CFs synergistically functioned. We believe this work will open up an opportunity to develop more metal vanadates materials as anodes for high-performance SIBs.

Acknowledgments

The authors acknowledge the financial support from European Research Council (ThreeDsurface: 240144), BMBF (ZIK-3DNanoDevice: 03Z1MN11), BMBF (Meta-ZIK-BioLithoMorphie: 03Z1M511), Volkswagen-Stiftung (Herstel-lung funktionaler Oberfl ächen: I/83 984).

References

[1] J. B. Goodenough, Y. Kim, Chem. Mater. 22 (2010) 587-603.

[2] M. Armand, J. M. Tarascon, Nature 451 (2008) 652-657.

[3] M. R. Palacin, Chem. Soc. Rev. 38 (2009) 2565-2575.

[4] V. Palomares, P. Serras, I. Villaluenga, K. Hueso, J. Carretero-Gonzalez, T. Rojo, Energy Environ. Sci. 5 (2012) 5884-5901.

[5] S. Ong, V. Chevrier, G. Hautier, A. Jain, C. Moore, S. Kim, X. Ma, G. Ceder, Energy Environ. Sci. 4 (2011) 3680-3688.

[6] N. Yabuuchi, K. Kubota, M. Dahbi, S. Komaba, Chem. Rev. 114 (2014) 11636-11682.

[7] S. Y. Hong, Y. Kim, Y. Park, A. Choi, N. S. Choi, K. T. Lee, Energy Environ. Sci. 6 (2013) 2067-2081.

[8] Y. Cao, L. Xiao, W. Wang, D. Choi, Z. Nie, J. Yu, L. V. Saraf, Z. Yang, J. Liu, Adv. Mater. 23 (2011) 3155-3160.

[9] N. Yabuuchi, M. Kajiyama, J. Iwatate, H. Nishikawa, S. Hitomi, R. Okuyama, R. Usui, Y. Yamada, S. Komaba, Nat. Mater. 11 (2012) 512-517.

[10] A. Abouimrane, W. Weng, H. Eltayeb, Y. Cui, J. Niklas, O. Poluektov, K. Amine, Energy Environ. Sci. 5 (2012) 9632-9638.

[11] S. Tepavcevic, H. Xiong, V. R. Stamenkovic, X. Zuo, M. Balasubramanian, V. B Prakapenka, C. S. Johnson, T. Rajh, ACS Nano 6 (2012) 530-538.

[12] Z. Wang, L. Qie, L. Yuan, W. Zhang, X. Hu, Y. Huang, Carbon 55 (2013) 328-334.

[13] Y. Cao, L. Xiao, M. L. Sushko, W. Wang, B. Schwenzer, J. Xiao, Z. Nie, L. V. Saraf, Z. Yang, J. Liu, Nano Lett. 12 (2012) 3783-3787.

[14] D. A. Stevens, J. R. Dahn, J. Electrochem. Soc. 147 (2000) 1271-1273.

[15] K.-T. Kim, G. Ali, K. Y. Chung, C. S. Yoon, H. Yashiro, Y.-K. Sun, J. Lu, K. Amine, S.-T. Myung, Nano Lett. 14 (2014) 416-422.

[16] Y. Xu, E. M. Lotfabad, H. Wang, B. Farbod, Z. Xu, A. Kohandehghan, D. Mitlin, Chem. Commun. 49 (2013) 8973-8975.

[17] H. Xiong, M. D. Slater, M. Balasubramanian, C. S. Johnson, T. Rajh, J. Phys. Chem. Lett. 2 (2011) 2560-2565.

[18] J. Qian, Y. Chen, L. Wu, Y. Cao, X. Ai, H. Yang, Chem. Commun. 48 (2012)

7070-7072.

[19] G. Yang, H. Cui, G. Yang, C. Wang, ACS Nano 8 (2014) 4474-4487.

[20] D. Choi, G. E. Blomgren, P. N. Kumta, Adv. Mater. 18 (2006) 1178-1182.

[21] H. Liu, W. Yang, Energy Environ. Sci. 4 (2011) 4000-4008.

[22] S. Hartung, N. Bucher, V. S. Nair, C. Y. Ling, Y. Wang, H. E. Hoster, M. Srinivasan, ChemPhysChem 15 (2014) 2121-2128.

[23] A. Moretti, F. Maroni, I. Osada, F. Nobili, S. Passerini, ChemElectroChem 2 (2015) 529-537.

[24] H. He, G. Jin, H. Wang, X. Huang, Z. Chen, D. Sun, Y. Tang, J. Mater. Chem. A 2 (2014) 3563-3570.

[25] D. Su, G. Wang, ACS Nano 7 (2013) 11218-11226.

[26] S. Tepavcevic, H. Xiong, V. R. Stamenkovic, X. Zuo, M. Balasubramanian, V. B. Prakapenka, C. S. Johnson, T. Rajh, ACS Nano 6 (2012) 530-538.

[27] X. Sun, J. Wang, Y. Xing, Y. Zhao, X. Liu, B. Liu, S. Hou, CrystEngComm 13 (2011) 367-370.

[28] D. Su, S. Dou, G. Wang, Chem. Commun. 50 (2014) 4192-4195.

[29] L. Liang, H. Liu, W. Yang, Nanoscale 5 (2013) 1026-1033.

[30] L. Liang, H. Liu, W. Yang, J. Alloy Compd. 559 (2013) 167-173.

[31] L. Liang, Y. Xu, Y. Lei, H. Liu, Nanoscale 4 (2014) 3536-3539.

[32] S. Zhang, L. Ci, H. Liu, J. Phys. Chem. C 113 (2009) 8624-8629.

[33] Y. Mao, H. Duan, B. Xu, L. Zhang, Y. S. Hu, C. C. Zhao, Z. X. Wang, L. Q. Chen, Y. S. Yang, Energy Environ. Sci. 5 (2012) 7950-7955.

[34] X. Zhou, Y. Zhong, M. Yang, M. Hu, J. Wei, Z. Zhou, Chem. Commun. 50 (2014) 12888-12891.

[35] Y. Xu, X. Han, L. Zheng, S. Wei, Y. Xie, Dalton Trans. 40 (2011) 10751-10757.

[36] H. Ma, S. Zhang, W. Ji, Z. Tao, J. Chen, J. Am. Chem. Soc. 130 (2008) 5361-5367.

[37] B. Luo, B. Wang, X. Li, Y. Jia, M. Liang, L. Zhi, Adv. Mater. 24 (2012) 3538-3543.

[38] C. He, S. Wu, N. Zhao, C. Shi, E. Liu, J. Li, ACS Nano 7 (2013) 4459-4469.

[39] Y. Xu, E. M. Lotfabad, H. Wang, B. Farbod, Z. Xu, A. Kohandehghan, D. Mitlin, Chem. Commun. 49 (2013) 8973-8975.

[40] Y. Cao, L. Xiao, M. L. Sushko, W. Wang, B. Schwenzer, J. Xiao, Z. Nie, L. V. Saraf, Z. Yang, J. Liu, Nano Lett. 12 (2012) 3783-3787.

[41] Z. Wang, L. Qie, L. Yuan, W. Zhang, X. Hu, Y. Huang, Carbon 55 (2013) 328-334.

[42] D. Su, H.-J. Ahn, G. Wang, Chem. Commun. 49 (2013) 3131-3133.

[43] Y. Park, D.-S. Shin, S. H. Woo, N. S. Choi, K. H. Shin, S. M. Oh, K. T. Lee, S. Y. Hong, Adv. Mater. 24 (2012) 3562-3567.

[44] W. Wang, C. Yu, Z. Lin, J. Hou, H. Zhu, S. Jiao, Nanoscale 5 (2013) 594-599.

[45] C.Wang, Y. Xu, Y. Fang, M. Zhou, L. Liang, S. Singh, H. Zhao, A. Schober, Y. Lei, J. Am. Chem. Soc. 137 (2015) 3124-3130.

[46] Y. Xu, X. Han, L. Zheng, W. Yan, Y. Xie, J. Mater. Chem. 21 (2011) 14466-14472.

List of Figures

Fig. 5 (a) Cycling performance of CuVOH-NWs/CFs composite, CuVOH-NWs, and CFs at a current density of 0.5 A g^{-1}. (b) Nyquist plots of CuVOH-NWs/CFs composite and CuVOH-NWs at open potential before cycling. (c) Galvanostatic charge/discharge curves of CuVOH-NWs/CFs composite anode at a current density of 0.5 A g^{-1}. (d) Rate cycle capability of CuVOH-NWs/CFs composite at various current densities from 0.1 to 10 A g^{-1}.

Fig. 6 SEM images of CuVOH-NWs/CFs composite after 100 cycles at a high current density of 0.5 A g^{-1}.

Table 1 Electrochemical performance comparison of the as-prepared CuVOH-NWs/CFs composite with some previously reported SIBs anodes.

Materials	Current density ($A\ g^{-1}$)/upper cut-off voltage	Discharge Capacity ($mAh\ g^{-1}$)		Rate capability, $mAh\ g^{-1}$ (current density, $A\ g^{-1}$)
		2^{nd} cycle	50^{th} cycle	
Carbon coated nanorod TiO_2[15]	0.01/3 V	~200	~190	~88 (1.65)
Nanocrystalline TiO_2[39]	0.05/2.5 V	~190	~160	~40 (2)
Hollow carbon nanowires[40]	0.05/1.2 V	~270	~250	~149 (0.5)
N-doped carbon nanofibers[41]	0.05/2.0 V	~170	~150	~87 (10)
SnO_2/RGO nanocomposite[42]	0.1/3.0 V	~380	~320	~125 (1)
Disodium terephthalate[43]	0.03/2.0 V	~310	~280	~100 (0.3)
WS_2/graphene nanocomposite[28]	0.32/3 V	~300	~260	~140 (0.64)
Microspheric $Na_2Ti_3O_7$[44]	0.354/2.5 V	~270	~170	~100 (3.54)
sodium 4,4'-stilbene-dicarboxylate[45]	0.05/2.5 V	~305	~200	~72 (10)
CuVOH-NWs/CFs composite	0.5/3 V	~399	~288	~207 (5)
	1	~356	~252	~128 (10)

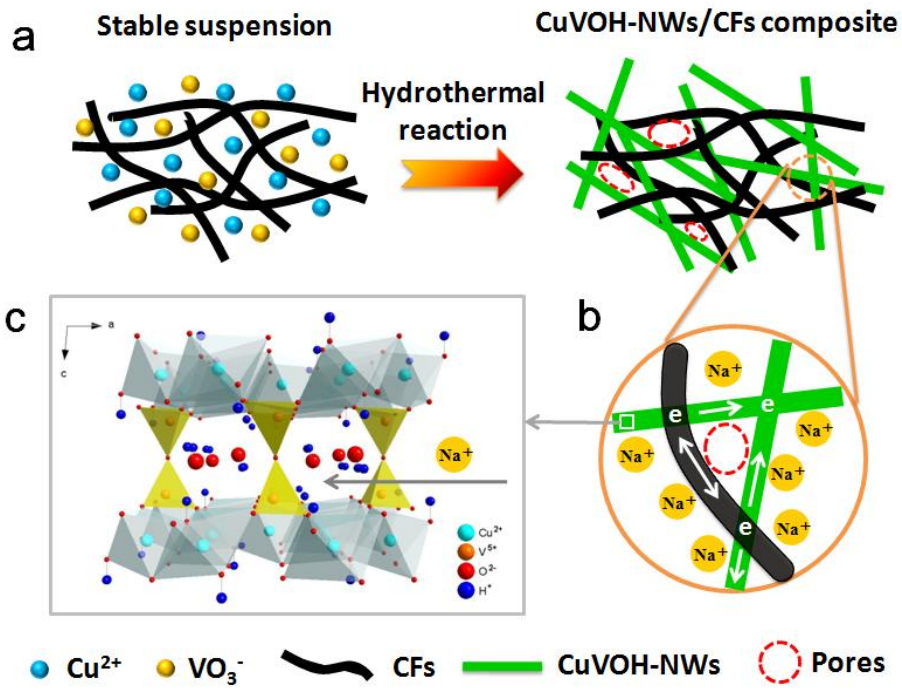
a
Stable suspension
CuVOH-NWs/CFs composite
Hydrothermal reaction
c
b
Na+
e
Cu2+
V5+
O2-
H+
Cu2+
VO3-
CFs
CuVOH-NWs
Pores

Scheme 1

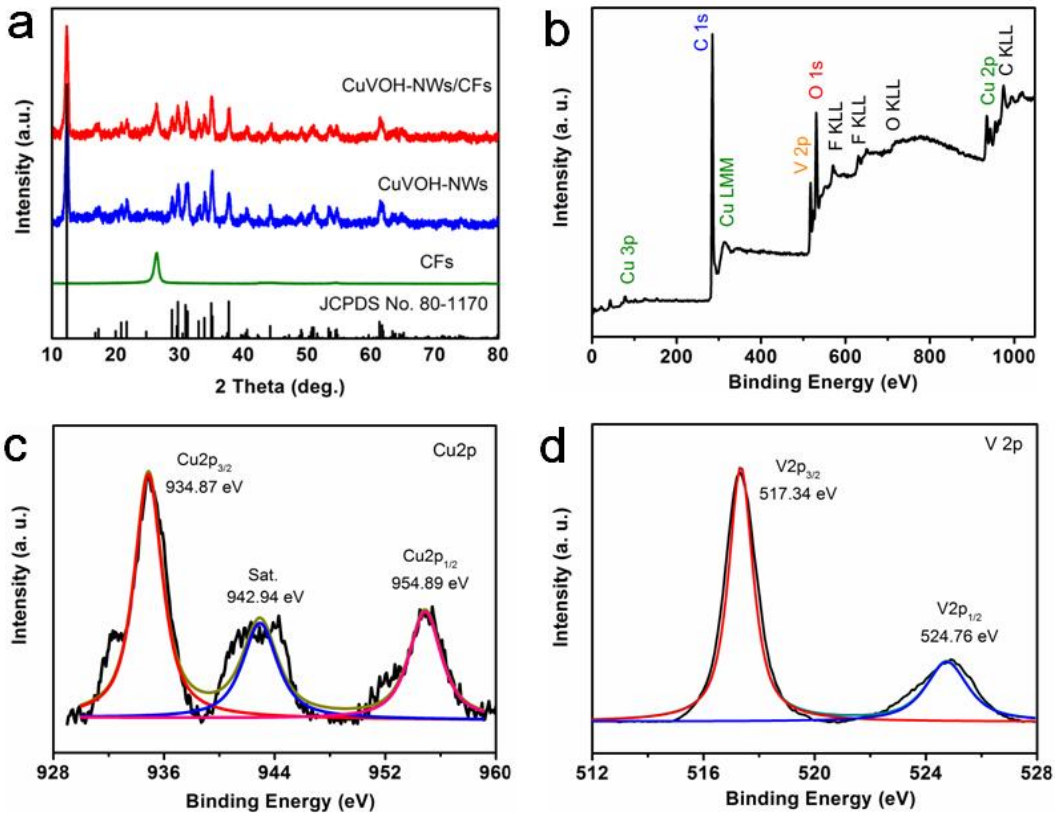
a
CuVOH-NWs/CFs
CuVOH-NWs
CFs
JCPDS No. 80-1170
Intensity (a.u.)
2 Theta (deg.)
b
C 1s
Cu LMM
V 2p
O 1s
F KLL
F KLL
O KLL
Cu 2p
C KLL
Cu 3p
Intensity (a. u.)
Binding Energy (eV)
c
Cu2p
Cu2p3/2
934.87 eV
Sat.
942.94 eV
Cu2p1/2
954.89 eV
Intensity (a. u.)
Binding Energy (eV)
d
V 2p
V2p3/2
517.34 eV
V2p1/2
524.76 eV
Intensity (a. u.)
Binding Energy (eV)

Fig. 1

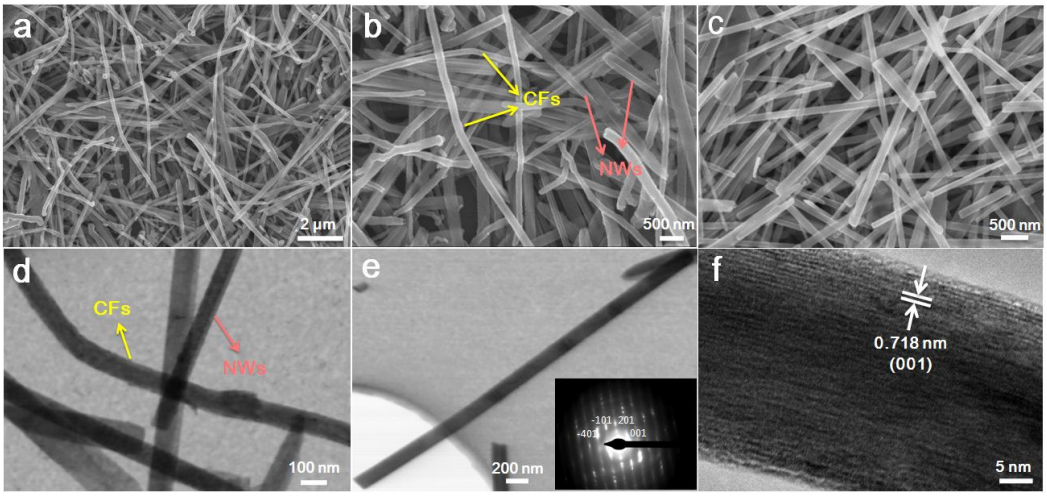
a
2 μm
b
CFs
NWs
500 nm
c
500 nm
d
CFs
NWs
100 nm
e
200 nm
-101
201
-401
001
f
0.718 nm
(001)
5 nm

Fig. 2

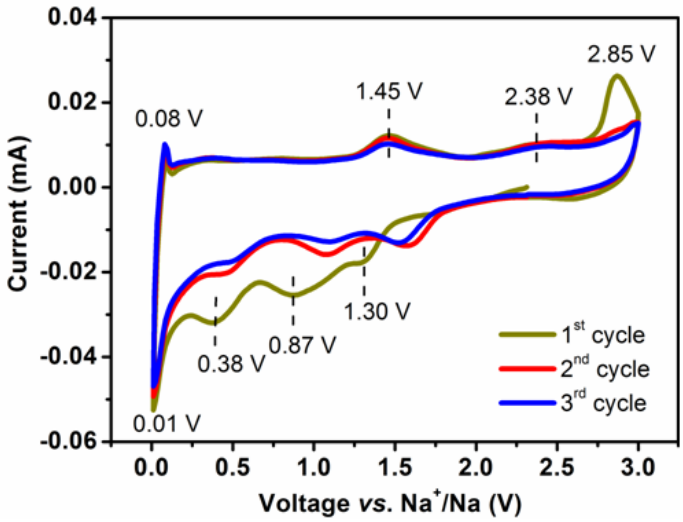
0.04
0.02
0.00
-0.02
-0.04
-0.06
Current (mA)
0.0
0.5
1.0
1.5
2.0
2.5
3.0
Voltage vs. Na+/Na (V)
0.08 V
1.45 V
2.38 V
2.85 V
0.38 V
0.87 V
1.30 V
0.01 V
1st cycle
2nd cycle
3rd cycle

Fig. 3

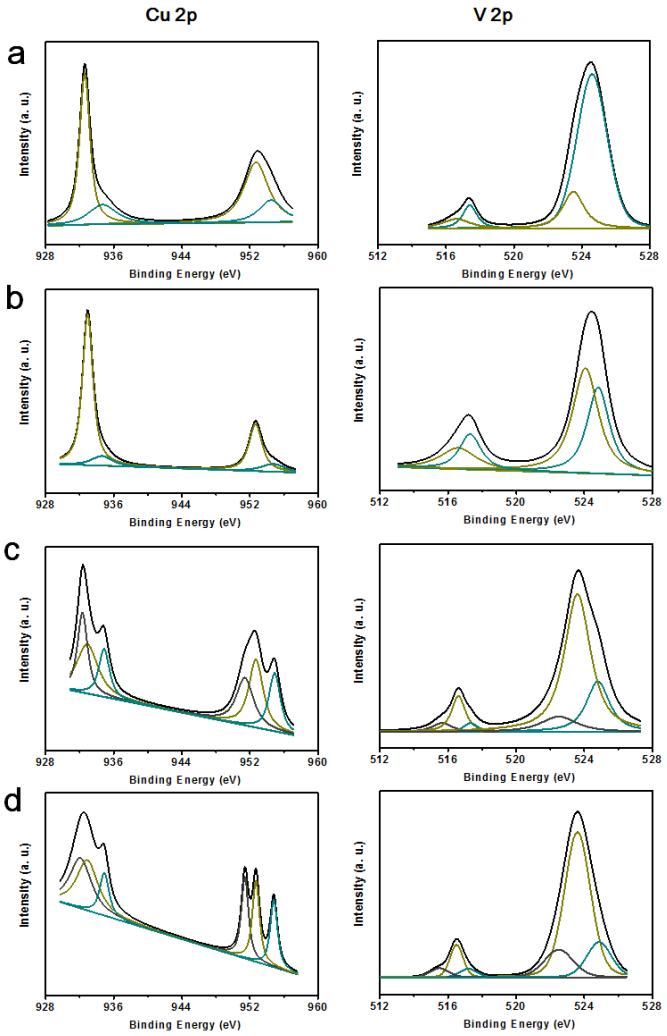
Cu 2p
V 2p
a
b
c
d
Intensity (a. u.)
Binding Energy (eV)
928
936
944
952
960
512
516
520
524
528

Fig. 4

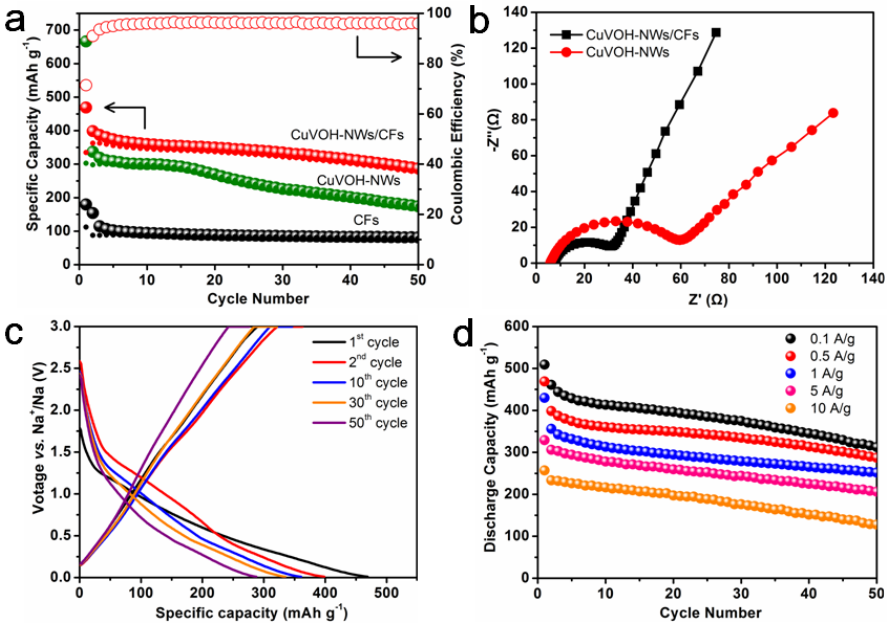
a
Specific Capacity (mAh g-1)
Coulombic Efficiency (%)
Cycle Number
CuVOH-NWs/CFs
CuVOH-NWs
CFs
b
-Z''(Ω)
Z' (Ω)
CuVOH-NWs/CFs
CuVOH-NWs
c
Votage vs. Na+/Na (V)
Specific capacity (mAh g-1)
1st cycle
2nd cycle
10th cycle
30th cycle
50th cycle
d
Discharge Capacity (mAh g-1)
Cycle Number
0.1 A/g
0.5 A/g
1 A/g
5 A/g
10 A/g

Fig. 5

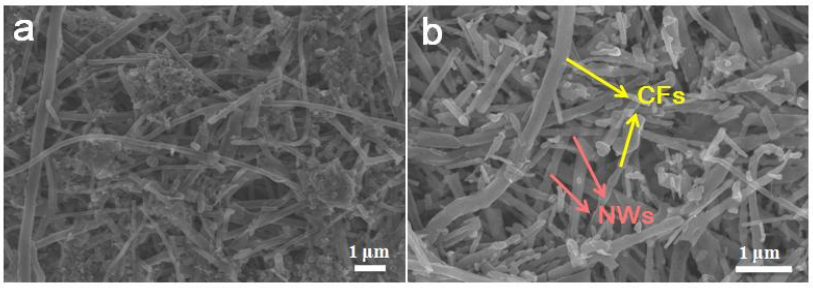

Fig. 6